U@C_s(4)-C_{82}: A Different Cage Isomer with Reactivity Controlled by U-Sumanene Interaction

Qin Wang,[†,⊥] Laura Abella,[§,⊥] Yang-Rong Yao,[‡] Yingjing Yan,[†] Daniel Torrens,[§] Qingyu Meng,[†] Shangfeng Yang,[‡] Josep M Poblet,[§] Antonio Rodríguez-Fortea,[§] and Ning Chen[†,]**

[†] College of Chemistry, Chemical Engineering and Materials Science, and State Key Laboratory of Radiation Medicine and Protection, Soochow University, Suzhou, Jiangsu 215123, P. R. China

[§] Departament de Química Física i Inorgànica. Universitat Rovira i Virgili, Marcel·lí Domingo 1, 43007 Tarragona, Spain

[‡] Department of Materials Science and Engineering, CAS Key Laboratory of Materials for Energy Conversion, Anhui Laboratory of Advanced Photon Science and Technology, University of Science and Technology of China, Hefei 230026, P. R. China

Keywords: *Actinide. Endohedral fullerene. Uranium. Reactivity.*

ABSTRACT: Actinide endohedral metallofullerenes (EMFs) are a fullerene family that possess unique actinide-carbon cage host-guest molecular and electronic structures. In this work, a novel actinide EMF, U@C_s(4)-C_{82}, was successfully synthesized and characterized, and its chemical reactivity was investigated. Crystallographic analysis show that U@C_s(4)-C_{82}, a new isomer of

U@C_{82}, has a C_s(4)-C_{82} cage, which has never been discovered in the form of empty or endohedral fullerenes. Its unique chemical reactivities were further revealed through Bingel-Hirsch reaction and carbene addition reaction studies. The Bingel-Hirsch reaction of U@C_s(4)-C_{82} shows exceptionally high selectivity and product yield, yielding only one addition adduct. Moreover, the addition sites for both reactions are unexpectedly located on adjacent carbon atoms far away from the actinide metal, despite the nucleophilic (Bingel-Hirsch) and electrophilic (carbene addition) nature of either reactant. DFT calculations suggest that this chemical behavior, unprecedented for EMFs, is directed by the unusually strong interaction between U and the sumanene motif of the carbon cage in U@C_s(4)-C_{82}, which makes the energy increase when it is disrupted. This work reveals remarkable chemical properties of actinide EMFs originating from their unique electronic structures and highlights the key role of actinide-cage interactions in the determination of their chemical behaviors.

Introduction

Endohedral fullerenes are fullerene molecules with unique host-guest structures. Various kinds of species, such as metal ions, nonmetal atoms, metal clusters or small molecules, can be encapsulated into hollow fullerenes.[1-4] To date, most reported endohedral fullerenes are endohedral metallofullerenes (EMFs). These EMFs have very diverse endohedral structures, which include various numbers of metal ions as well as versatile metal clusters.[1,3] The most fascinating features of EMFs are the interaction between the encaged species and fullerenes. The charge transfer and coordination effect between the encaged metal ions and carbon cages can essentially alter the electronic structures of the parent fullerene cages.[2-3,5] On the other hand, the chemical or physical

modification of the fullerene cages can effectively penetrate the carbon cage and alter the motion and electronic structures of the endohedral species.[1,6] This unique interaction between the host fullerene cages and the guest endohedral species endows EMFs with some unique applications in the fields of biomedicine and molecular electronic devices.[1,7-11]

Chemical derivation of EMFs is essential for their applications, as it can adjust their electronic structures, solubility and biocompatibility.[1,12] However, the reactivity of EMFs is far more complicated than that of empty fullerenes due to the relatively low molecular symmetry and the influence of the encapsulated species. These reactions often yield multiple fullerene derivatives, which cause significant difficulties in purification processes and thus result in low yields of the target compound. Thus, understanding the role of metal-cage interactions on the reactivity of EMFs is desirable for tuning their chemical reactivity.

To date, the understanding of the chemical properties of EMFs is still underdeveloped, as only a few types of chemical reactions have been reported, such as silylation reactions, Bingel-Hirsch (BH) reactions, Diels-Alder reactions, radical recombination reactions, Prato reactions and carbene reactions.[1,6,13] Previous studies have shown the size effect of endohedral clusters on the chemical reactivity of EMFs,[14] but the role of the nature of the metal ions themselves has rarely been discussed, partially due to the very similar chemical behaviors of EMFs with endohedral lanthanides.[1,13]

Actinide EMFs have unique molecular and electronic structures that are significantly different from those of lanthanide EMFs.[15-18] For example, Th@C_{82} shows a unique four-electron metal-cage charge transfer, while for U@C_{2n}, the valence states of actinides are variable and can be dictated by the variable isomeric structures of fullerene carbon cages.[16,19] Our very recent reaction study of Th@C_{3v}(8)-C_{82} and U@C_{2v}(9)-C_{82} shed light on their unusual chemical reactivities and showed that

their reactivities are different from those of their lanthanide analogs.[20] Nevertheless, the chemical reactivity of actinide EMFs remains largely unexplored.

Herein, we report the synthesis and chemical reactivity studies of a novel actinide mono-EMF: U@C_s(4)-C_{82}. The molecular structure of U@C_s(4)-C_{82} was unambiguously determined by X-ray single crystal crystallography, and its chemical reactivities were investigated through the Bingel-Hirsch reaction and carbene addition reaction. Unexpected reactivity is found for U@C_s(4)-C_{82}, with uncommonly high regioselectivity for both studied reactions. In particular, the adducts of both reactions show the reaction addition sites located on adjacent carbon atoms far from the U atom, despite their nucleophilic and electrophilic nature, respectively.

Results and Discussion

Synthesis and Isolation of U@C_s(4)-C_{82}. Uranium endohedral metallofullerenes were produced by a modified Krätschmer–Huffman DC arc discharge method. Graphite rods packed with U_3O_8 and graphite powder (molar ratio of U: C = 1:30) were vaporized in the arcing chamber under a 200 Torr He atmosphere and 4 Torr N_2. The resulting soot was then collected and extracted with CS_2 for 12 h. Multistage high-performance liquid chromatography (HPLC) separation processes were employed to isolate and purify U@C_{82} (Figure S1). The purity of the sample was confirmed by the observation of a single peak by HPLC and positive-ion-mode matrix-assisted laser desorption-ionization time-of-flight mass spectrometry (MALDI-TOF MS). As shown in Figure 1, the mass spectrum of the purified U@C_s(4)-C_{82} shows a peak at m/z = 1221.929. In addition, the experimental isotopic distributions of the sample agree well with the theoretical predictions.

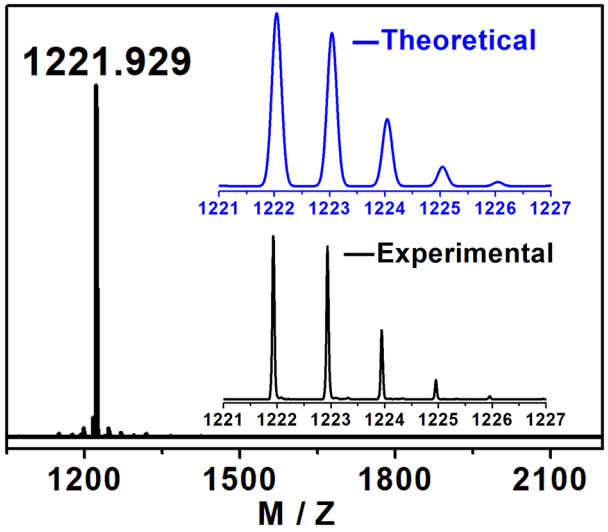

Figure 1. Positive-ion mode MALDI-TOF mass spectrum of U@C_{82} and the expansions of the corresponding experimental isotopic distributions of the compound in comparison with its calculated ones.

The molecular structure of U@C_s(4)-C_{82} was unambiguously determined by single-crystal X-ray diffraction analysis. U@C_s(4)-C_{82} was cocrystallized with Ni^{II}(OEP) (OEP = 2, 3, 7, 8, 12, 13, 17, 18-octaethylporphyrin dianion) by slow diffusion of the benzene solution of Ni^{II}(OEP) into the carbon disulfide solution of the purified compound. Theoretical calculations of the relative formation energies for nine pristine isolated pentagon rule (IPR) C_{82} isomers revealed that C_2(3)-C_{82} is the most stable pristine C_{82} isomer, followed by isomers C_s(4), C_s(2), and C_2(1), whereas the pristine isomers, i.e., C_{3v}(7), C_{3v}(8), and C_{2v}(9) appeared to be extremely unstable.[21-22] To date, five isomeric structures of C_{82}, C_2(5)-C_{82}, C_s(6)-C_{82}, C_{3v}(7)-C_{82}, C_{3v}(8)-C_{82}, and C_{2v}(9)-C_{82}, have been obtained experimentally in the form of endohedral fullerenes. C_2(5)-C_{82} and C_2(3)-C_{82} can be transformed into the C_s(4)-C_{82} structure by a one-step Stone-Wales (SW) rearrangement. However, C_s(4) has never been obtained in its pristine form either as an empty cage or in the form of endohedral fullerene. The only experimental report of C_s(4)-C_{82} is C_s(4)-$C_{82}Cl_{20}$, a distorted cage structure after

chlorination.[23] Thus, U@C_s(4)-C_{82}, to the best of our knowledge, is the first observation of pristine C_s(4)-C_{82} stabilized by the encapsulation of U.

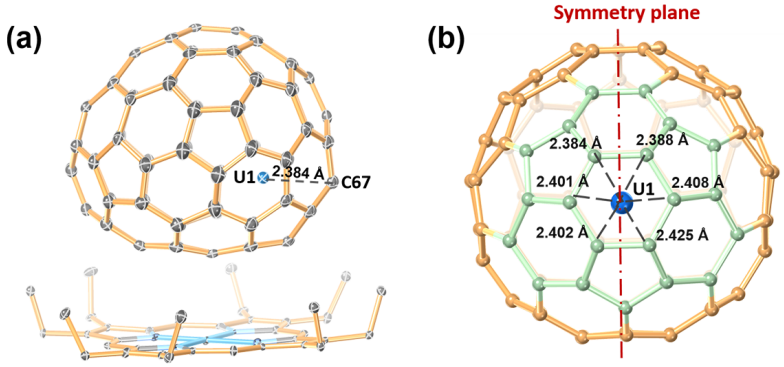

Figure 2. (a) ORTEP drawing showing the relationship between the EMFs and porphyrin moiety for U@C_s(4)-C_{82} with 15% thermal ellipsoids; only the major uranium site (U1 with 0.697 occupancy) is shown. For clarity, the solvent molecules and minor metal sites are omitted. (b) View showing the interaction of the metal ion (major metal site) with the closest cage portion. The symmetry plane is highlighted with dotted red lines. The sumanene motif closest to the encapsulated metal ions is highlighted in light green.

Inside the cage, five crystallographic sites for U atoms can be identified. The major site of U has an occupancy value of 0.697 (U1), and the minor sites have much smaller occupancy values of 0.120 (U2), 0.057 (U3), 0.034 (U4), and 0.092 (U5), suggesting that the U ion is largely ordered inside the cage. As shown in Figure 2b, the major U site, i.e., U1 lies over a cage carbon (C67) at the apex between two hexagons and one pentagon with a short U-C distance of 2.384 Å, near a sumanene motif, which is in good agreement with the density functional theory (DFT) calculations (see Figure S5). This is consistent with the previous observation that U atoms tend to be located near sumanene patterns.[18] Different positions of the metal within the C_s(4)-C_{82} cage were calculated to analyze the most likely location of the metal inside the C_s(4)-cage (Figure S5c). The U atom located near the sumanene is found to be by far the lowest-energy structure, in agreement with the

X-ray structure, followed by the position lying next to the double jointly sumanene pattern at 20 kcal·mol^{-1}. Other positions lay at much higher energies (30 kcal·mol^{-1}), which confirms the high stability of U placed in the symmetry plane next to the sumanene motif. In addition, to confirm the high stability of U@C_s(4)-C_{82}, our calculations show that U@C_s(4)-C_{82} is among the lowest-energy and most abundant isomers among the nine IPR C_{82} cages (Figure S6).

The electronic structure of U@C_s(4)-C_{82} in its spin-triplet ground state is consistent with a formal oxidation state of U(+4). This is confirmed by a) the molecular orbital analysis (Figure S5); and b) the spin population of ~2 unpaired electrons in the U center (f^2). It is remarkable that the C_s(4)-C_{82}^{4-} tetra-anion is at very high energy (around 30 kcal mol^{-1}) compared to the lowest-energy C_{3v}(8)-C_{82}^{4-} tetra-anion. Therefore, the high stability of U@C_s(4)-C_{82} with respect to other U@C_{82} isomers comes from the *particular* interaction between the actinide and the sumanene motif in this cage and cannot be explained by the so-called ionic model, which is so successful in lanthanide EMFs.

Chemical reactivity studies of U@C_s(4)-C_{82}

U@C_s(4)-C_{82}C(COOC$_2$H$_5$)$_2$. The Bingel reaction of U@C_s(4)-C_{82} with an excess amount of diethyl bromomalonate (**1**) was carried out in the presence of 1,8-diazabicyclo[5.4.0]-undec-7-ene (DBU) in anhydrous toluene under an argon atmosphere at room temperature.[24-26] The reaction process was monitored by high-performance liquid chromatography (HPLC). Figure 3 shows the reaction scheme and the corresponding HPLC profiles of the reaction mixture probed at different times.

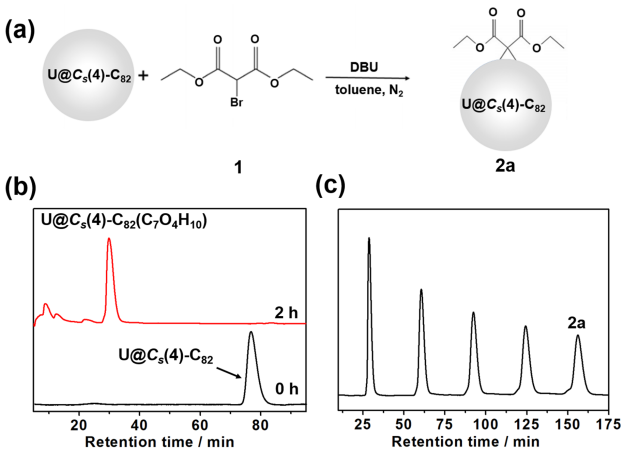

Figure 3. (a) Schematic illustration of the Bingel–Hirsch reaction of U@C_s(4)-C_{82} with (**1**) in the presence of 1,8-diazabicyclo[5.4.0]-undec-7-ene (DBU). (b) HPLC profiles of the reaction mixture probed at different times. (c) Recycling HPLC profile for the separation of **2a**. HPLC conditions: Buckyprep column (10 mm × 250 mm), eluent = toluene, flow rate = 4 mL min^{-1}; detection wavelength = 310 nm.

The single peak at retention time of 80 min can be assigned to the unreacted pristine U@C_s(4)-C_{82}. After the reaction proceeded for 2 h, a new peak of mono-adduct (**2a**) was observed at 27 min, as confirmed by mass spectrometry results (*m/z* =1380.057 (Figure S2). A recycling HPLC separation process was then employed to verify the purity of this mono-adduct. After five recycling steps (Figure 3c), the peak of **2a** is still a well-defined single peak. This suggests that the Bingel-Hirsch reaction of U@C_s(4)-C_{82} with **1** only afforded one mono-adduct isomer. In addition to its high regioselectivity, the product yield of **2a** reaches as high as 72%.

Extensive studies on the Bingel-Hirsch reaction of endohedral fullerenes have been carried out for variable EMFs, including mono-EMFs such as M@C_{2v}(9)-C_{82} (M= La, Gd),[27-30] Y@C_s(6)-C_{82},[31] and metallic nitride clusterfullerenes (NCFs) such as M_3N@I_h(7)-C_{80} (M=Sc, Y, Gd, Lu, Er)[14, 32-34], Gd_3N@C_{2n} (2n=82, 84, 88)[35-36] and TiM_2N@I_h (7)-C_{80} (M=Sc, Y)[37-38]. Notably, most of these Bingel-Hirsch reactions yield more than one mono-adduct. Some EMFs, i.e., Sc_3N@C_{68}[39] and Sc_3N@C_{78}[40]

yield one mono-adduct but multiple adducts. Thus, both the regioselectivity of the Bingel reaction of U@C_s(4)-C_{82} and the yield of **2a** are exceptionally high compared to the known EMFs.

The molecular structure of **2a** was further determined by single-crystal X-ray diffraction (XRD) analysis. Black crystals of **2a** were obtained by slow evaporation of a solution of **2a** in carbon disulfide (CS_2) with *n*-hexane layered above. Inside the cage, the U atom exhibits three disordered positions with fractional occupancy values of 0.780 (U1), 0.107 (U1A), and 0.113 (U2). The fullerene cage is completely ordered. As shown in Figure 4, the addition occurred at a [6,6] ring junction, which is common for methano-adducts of fullerenes via the Bingel-Hirsch reaction. The attached malonate group is far from where the U atom is located, consistent with what has been observed for the previous reaction studies of M@C_{82} (M=Gd, Y, and La)[31,41,29-30,42] that the nucleophilic bromomalonate reactant prefers to attach at the region far from the internal metal ion of mono-EMFs.

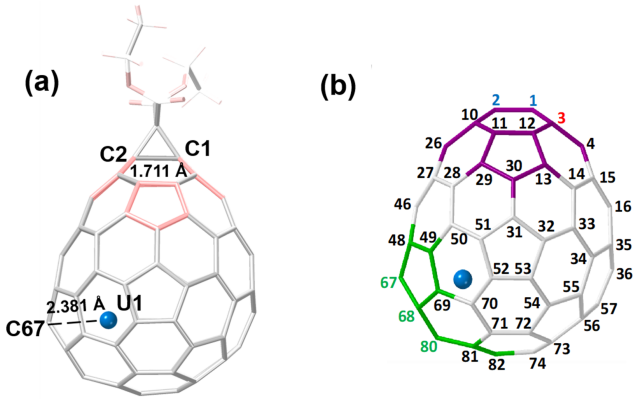

Figure 4. (a) Experimental structure of U@C_s(4)-$C_{82}C(COOC_2H_5)_2$ (front) (**2a**). (b) Labels for the different carbon atoms of M@C_s(4)-C_{82} (M=Th, U). The sumanene motif where the metal atom is located is drawn in green, and the region where the reaction takes place is drawn in purple.

The Bingel–Hirsch reaction is an important nucleophilic [2+1] cycloaddition that generates a three-membered ring on the fullerene surface. Three addition patterns have been reported for the

BH reaction of EMFs to date.[14,27-36,39-40,43] One of them is the closed cage of the cyclopropane addition mode, which was reported in the reaction of Gd@C_{2v}(9)-C_{82},[27-28] Sc_3N@C_{78}[40] and Gd@C_{60}.[12] However, to date, there is no unambiguous crystallographic proof of the closed cages of these cyclopropane adducts. In this work, surprisingly, crystallographic analysis unambiguously shows that **2a** has a [6,6] closed structure with a C1-C2 distance of 1.711 Å, which represents the first crystal structure of the closed ring of the Bingel-Hirsch adduct of EMFs. The nearest U-to-cage distance in **2a** is 2.381 Å (*vs*. 2.394 Å in calculations, Figure S7), which is slightly shorter than the value in pristine U@C_s(4)-C_{82} (2.384 Å), suggesting a likely slight change in the U-cage interaction as a consequence of the BH reaction.

The BH reaction proceeds by a two-step mechanism (Figure S3).[44] First, the bromomalonate reacts with the fullerene cage by nucleophilic addition to form a negatively charged intermediate. Then, the carbanion displaces the bromide, and an intramolecular cyclopropane ring closure takes place. Recently, a predictive aromaticity criterion (PAC) for BH reactions was proposed, which suggests that the addition of EMFs should occur at particular sites to maintain the maximal aromaticity of the fullerene cages.[44] The first principle of PAC is that in the first step of the Bingel-Hirsch reaction, the lowest-energy intermediate should be located at a 666 C atom (i.e., a carbon atom situated among three hexagonal rings, denoted as C-666). However, the structure in the **2a** crystal does not follow the predictive aromaticity criteria at all. In fact, in this case, the addition occurs at a carbon atom C1 or C2 (see Figure 4), which are the carbon atoms situated among two hexagonal rings and one pentagonal ring (C-566).

A detailed DFT analysis for the BH reaction on U@C_s(4)-C_{82} to yield U@C_s(4)-$C_{82}C(COOC_2H_5)_2$ (**2a**) was performed. For many calculations, we have used the Th atom as a model for the U atom because of its simpler electronic structure without f electrons in the Th(IV) oxidation state. Due to

the low symmetry of the M@C_s(4)-C_{82} (M=Th, U) cage, the BH reaction could take place on up to 44 different carbon sites, see Figure 4b and Supporting Information (SI) for labels of equivalent atoms. Table 1 shows that the lowest-energy product is the adduct on bond 1-2 (denoted as B1-2, the same as experimental structure **2a**), followed by product B11-12, far from the metal site, at 4-5 kcal·mol^{-1} and product B67-68, in the sumanene near the metal, at 5-7 kcal·mol^{-1}. Some regioisomers are predicted to have energies as high as 30 kcal mol^{-1}. A complete list of all the results is collected in the SI (Table S4). Similar energies for Th and U are observed (Figure S9), confirming that our model with Th is suitable for the goal of this study.

Table 1. Relative Energies and C-C Distances for Different Bingel-Hirsch (BH) Reaction Products of M@C_s(4)-C_{82} (M=Th, U).[a]

Bond type	Bond X-Y[b]	Th@C_{82}BH		U@C_{82}BH	
		E_{rel}	d(X-Y)	E_{rel}	d(X-Y)
[6,6] - closed	1-2 (2a)	0.0	1.633	0.0	1.632
[5,6] - open	11-12	4.2	2.197	5.4	2.197
[5,6] - open	67-68	6.8	2.107	5.4	2.108
[6,6] - closed	28-29	7.4	1.654	9.2	1.650
[6,6] - open	32-33	7.9	2.147	8.0	2.146
[6,6] - closed	10-11	8.3	1.556	8.6	1.556
[6,6] - closed	13-14	8.7	1.716	8.6	1.703
[5,6] - open	79-80	8.9	1.938	10.3	1.971
[6,6] - closed	50-51	9.5	1.641	10.4	1.632
[5,6] - open	4-5	11.1	2.195	13.1	2.190
[6,6] - open	14-33	11.2	2.324	12.4	2.324
[5,6] - open	16-17	15.2	2.180	15.4	2.180
[6,6] - closed	30-31	15.5	1.510	15.2	1.508
[6,6] - open	68-80	15.7	2.184	15.9	2.163
[5,6] - open	1-3	16.0	2.139	16.3	2.141
[5,6] - open	10-26	16.5	2.165	16.5	2.160

[6,6] - closed	4-15	17.2	1.633	17.3	1.634
[5,6] - open	2-10	17.9	2.130	19.1	2.129
[6,6] - open	66-67	23.8	2.095	21.5	2.086
[5,6] - closed	68-69	24.2	1.588	28.2	1.668
[5,6] - closed	11-29	24.9	1.603	24.5	1.600
[6,6] - closed	56-57	28.6	1.628	29.4	1.628
[6,6] - closed	74-82	29.7	1.741	29.7	1.661

[a] Relative energies in kcal mol^{-1} and distances in Å, computed at the PBE0/TZP/D3 level. [b] Labels for the carbon atoms according to Figure 4b. The experimental structure (**2a**) corresponds to the addition on bond 1-2 (B1-2).

Table 2. Relative Energies with respect to Reactants for the Different Intermediates (I), Transition States (TS) and Products (P) of the Bingel-Hirsch Addition on Th@C_s(4)-C_{82}.[a]

I	Atom type	E_{rel} I	E_{rel} TS	Barrier	P	Bond type	E_{rel} P
I-1A	566	-27.2	-4.8	22.4	B1-3	[5,6]	-22.5
I-1B	566	-27.1	-18.1	9.0	B1-2	[6,6]	-38.4
I-2	566	-25.6	-18.2	7.4	B1-2	[6,6]	-38.4
I-29A	566	-22.9	-14.1	8.8	B28-29	[6,6]	-31.1
I-29B	566	-24.1	-1.7	22.4	B29-30	[5,6]	-13.8
I-29C	566	-23.0	-0.8	22.1	B11-29	[5,6]	-13.7
I-51	566	-27.6	-14.6	13.0	B50-51	[6,6]	-28.6

[a] Data from single-point calculations at the PBE0/COSMO level (toluene as solvent) using the PBE optimized geometry. Relative energies in kcal mol^{-1}.

The relative energies of different regioisomers are compatible with thermodynamic control of the reaction. However, previous studies suggest that BH reactions for most of the reported EMFs take place under kinetic control.[34, 42, 44-50] Thus, the kinetic aspects of the process computing the different stationary points in the reaction path are also investigated. In the first step, the

intermediate (I) is formed, and then, to reach the product, a transition state (TS) has to be overcome through an energy barrier.

Different intermediates for the addition of bromomalonate on M@C_s(4)-C_{82} (M=Th, U) were calculated using different computational settings (Table S5). In these intermediates, the malonate group is bonded to one C atom of the fullerene, named I-X in the text. The intermediate can present different conformations of the bromomalonate due to rotation around the C_{cage}-C_{mal} bond, distinguished as A, B, and C in the following, which can lead to different products. Two intermediates, I-1 and I-51, appear degenerate when the PBE functional is considered. Using PBE0, intermediate I-29 is also low in energy jointly with I-1 and I-51. Note that similar relative energies are obtained for Th and U, most of which are within 1 kcal mol^{-1}. These intermediates, I-1, I-51 and I-29, have been studied in the following steps of the BH reaction path, as well as I-2, which also appears low in energy and reaches product **2a**.

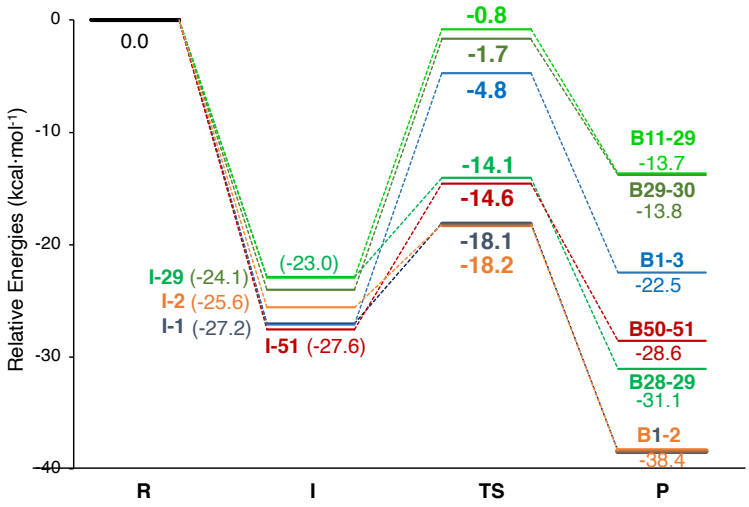

Figure 5. Energy profiles for the Bingel-Hirsch addition of bromomalonate on Th@C_s(4)-C_{82}, considering single point energy calculations at the PBE0 level and solvent effects (toluene) with the PBE optimized geometry. Red, blue, orange and green lines correspond to the I-51, I-1, I-2 and I-29 intermediates and, consequently, their reaction pathways. TS energies (in kcal·mol^{-1}) are

indicated. The barrier for the lowest-energy TS is 7.4 kcal mol^{-1}. The B1-2 product is the experimental structure **2a**.

The transition states for the selected intermediates have been determined and characterized, resulting in the TS from intermediates I-1B and I-2 having the lowest relative energy (see Table 2). Once I-1B or I-2 transition states are overcome, the final product **2a** is formed in each reaction path. The energy barriers are 7 and 9 kcal·mol^{-1} for I-1B and I-2, respectively, values that can be easily overcome at work temperatures. Figure 5 displays the energy profiles for the BH addition of bromomalonate on Th@C_s(4)-C_{82}, where it is clearly seen that the two TS that evolve to **2a** (B1-2) are those with the lowest relative energies and lowest barriers. Therefore, our results show that the formation of **2a** also takes place under kinetic control. It is worth noting that analogous results are obtained if we consider the free energy profile (Table S6), as well as for U@C_s(4)-C_{82} (Table S7).

Therefore, we have shown that the adduct on carbon bond 1-2 is by some kcal mol^{-1} the most favorable product in the BH reaction, in line with the high regioselectivity of the experiment. This result can be easily understood from qualitative frontier MO theory. In BH reactions, there is a nucleophilic attack of the malonate on the carbon cage. Analyzing the frontier molecular orbitals (MOs) of Th@C_s(4)-C_{82}, we found that carbon atoms 1 and 2 have the largest MO contribution to the lowest unoccupied MO (LUMO, Figure S10), which agrees with the formation of intermediate I-1. The frontier MOs of I-1 were also analyzed, as the second step is the rate determining step in the reaction (Figure S11). The largest MO contribution in the HOMO of I-1 lies on carbon atom 2, and a nonnegligible MO contribution in LUMO+2, almost degenerated with LUMO+1, is found in the C atom of the malonate attached to the carbon cage. This is in accordance with the formation

of product **2a**. Moreover, the pyramidalization angles of Th@C_s(4)-C_{82} show that the reaction takes place in the most distorted region far from the metal (Table S8).

U@C_s(4)-C_{82}Ad. The photochemical reaction of U@C_s(4)-C_{82} with AdN_2 was also carried out to further investigate the chemical reactivity of this novel actinide EMF. The toluene solution of U@C_s(4)-C_{82} with an excessive addition of AdN_2 was irradiated with an ultrahigh-pressure mercury-arc lamp (cutoff < 350 nm) at room temperature. The reaction was monitored by analytical HPLC (Figure 6). Before irradiation, only one HPLC peak of U@C_s(4)-C_{82} appeared at retention time of approximately 80 min. After irradiation for 20 min, approximately 80% of U@C_s(4)-C_{82} was consumed, and two new peaks appeared at 32 min and 37 min. Both of the mass spectra of these two HPLC fractions show a well-defined signal at m/z = 1356, which can be ascribed to the signal of the two mono-adduct isomers of U@C_s(4)-C_{82}Ad and agree well with the theoretical isotopic distribution (Figure S4). Thus, the resulting reaction products can be assigned to the mono-adduct isomers of U@C_s(4)-C_{82}Ad(I) and U@C_s(4)-C_{82}Ad(II), respectively. These mono-adducts were conveniently isolated and purified using a Buckyprep column. The conversion yields of U@C_s(4)-C_{82}Ad(I) and U@C_s(4)-C_{82}Ad(II) were calculated to be ca. 82% and ca. 18%, as estimated by their HPLC peak area.

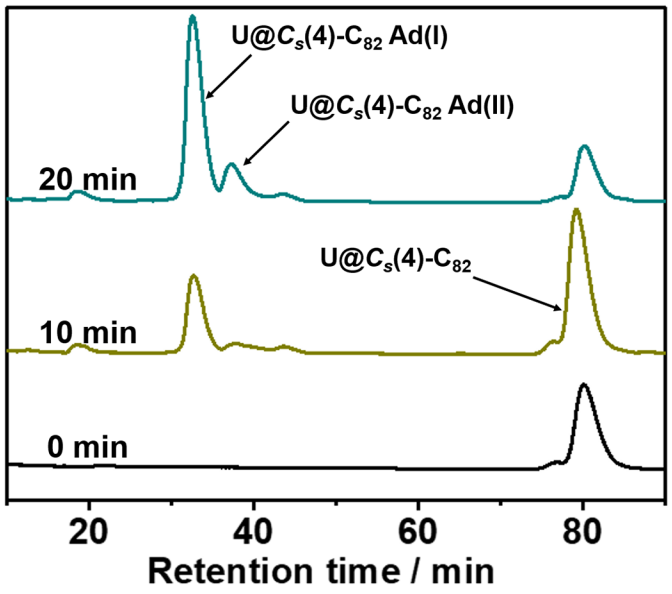

Figure 6. HPLC profiles of the reaction mixture probed at different reaction times (black line: 0 min, green line: 10 min, blue line: 20 min). HPLC conditions: Buckyprep column (10 mm × 250 mm), eluent = toluene, flow rate = 4 mL min^{-1}; detection wavelength = 310 nm.

The molecular structures of U@C_s(4)-C_{82}Ad(I) (racemic twins) were unambiguously determined by single-crystal X-ray diffraction analyses (Figure 7). Single crystals were obtained by layering hexane over a solution (*o*-dichlorobenzene/CS_2, v:v = 1:1) of the derivative in a glass tube. Inside the cage, the U atom is highly ordered, and only two disordered positions with fractional occupancy values of 0.892 (U1) and 0.108 (U1A) were observed. The addition occurred at the [5,6]-bond [C(1)–C(3)], and the C1-C3 distance increased to 2.080 Å (*vs*. 2.073 Å in calculations, Figure S12), which is notably longer than that of the typical C–C single bond (1.5 Å). The closest U-cage distance in U@C_s(4)-C_{82}Ad(I) is 2.350 Å (Figure 7a), slightly shorter than the value in pristine U@C_s(4)-C_{82} (2.384 Å). However, surprisingly, the U atom is far from the Ad group, which is different from the common understanding of electrophilic reactions in which the internal metal atom is located near the addition site, as observed in the corresponding reactions of M@C_{2v}(9)-C_{82} (U, Y, La, Ce, Gd, and Sc), La@C_s(6)-C_{82} and Th@C_{3v}(8)-C_{82}.[20,51-56] Nevertheless, this result is rather

similar to the case of Yb@C_2(13)-C_{84}, where the metal is placed under a hexagonal ring far from the sites of addition.[57] For this reaction, computational works suggested that the addition of Ad to Yb@C_2(13)-C_{84} is mainly driven by releasing the local strains of cage carbons rather than charge recombination due to the evenly distributed charge densities of divalent EMFs.[57] Likewise, we speculated that for U@C_s(4)-C_{82}, there may also be a stronger driving force than the electrophilic reactive sites on the fullerene cage.

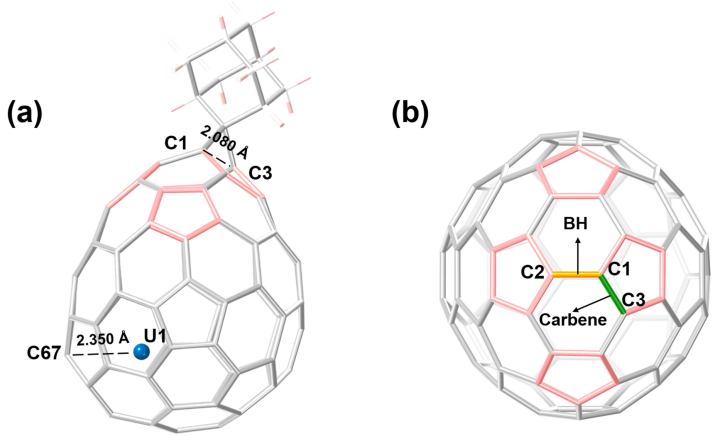

Figure 7. (a) The optimized structure of U@C_s(4)-C_{82}Ad(I) (Front). (b) Addition site of the Bingel-Hirsch (BH) and Carbene reactions (Top).

Thus, a computational study was also carried out to analyze carbene addition on U@C_s(4)-C_{82}. As in the BH reaction, we first proceeded with the model calculations on Th@C_s(4)-C_{82}. In previous reports, the local strain on cage carbons plays a key role in determining the reactivity of carbene addition.[20, 52, 54-56, 58-59] The pyramidalization angles from the π-orbital axis vector (POAV) are a useful tool for exploring the local strain. Nevertheless, it has also been shown that in some cases, the charge density is more effective than the POAV value to understand the carbene addition.[51, 53] Therefore, based on the largest pyramidalization angles (Table S8) and the largest negative Mulliken charge densities (Figure S13) of M@C_s(4)-C_{82} (M=Th, U), selected bonds were

considered to calculate the corresponding carbene products, which include, among many others, the experimental structure of U@C_s(4)-C_{82}Ad(I) (see Tables 3 and S9). The lowest-energy cycloadduct is that with the carbene attached to bond 1-2 (product B1-2). Interestingly, this is the same bond where the BH reaction takes place. Carbon atoms C1 and C2 show rather large POAV values and significantly large negative charges, suggesting that this bond is rather favorable for the electrophilic attack of the Ad group. Carbon atoms close to the metal, i.e., C80, C68 and C67 are also electron-rich sites. However, the relative energies of the corresponding products B68-80, B79-80 and B67-68 are found to be approximately 8 kcal·mol^{-1}. The crystallographic U@C_s(4)-C_{82}Ad(I) structure, which shows the Ad group attached to the 1-3 bond far from the metal (B1-3 product), is 18.7 kcal·mol^{-1} higher in energy than the lowest-energy B1-2 product. A test calculation on the B1-3 product with the metal close to the cycloadduct shows that the metal prefers to remain near the sumanene by 12 kcal·mol^{-1}. This is most likely due to the very favorable actinide-sumanene interaction in the U@C_s(4)-C_{82} cage, which restricts the actinide to be fixed at that position. Analogous results were found for M = Th and U (Table 3 and Figure S14).

Calculations on the mechanism of carbene addition were also conducted to further understand the observed addition position of Ad to the M@C_s(4)-C_{82} (M=Th, U) cage. In this case, preliminary calculations were performed with a model of the Ad group, i.e., we replaced it with the $C(CH_3)_2$ model. Then, selected structures were also recomputed with the Ad group. The carbene addition reaction is an electrophilic reaction that may take place via two pathways depending on the spin state of the carbene, i.e., singlet or triplet spin states. Both studied carbenes, the $C(CH_3)_2$ model and Ad group, show that the triplet spin state is somewhat lower in energy than the singlet configuration (Table S10). Thus, we first studied the carbene addition via the triplet carbene

reaction pathway in detail. However, the singlet carbene mechanism has also been analyzed due to the small relative energies between both spin states.

Table 3. Relative Energies and C-C Bond Distances of Selected Carbene Reaction Products of M@C_s(4)-C_{82} (M=Th, U).[a]

Bond type	Bond X-Y[b]	Th@C_{82}Ad		U@C_{82}Ad	
		E_{rel}	d(X-Y)	E_{rel}	d(X-Y)
[6,6] - closed	1-2	0.0	1.653	0.0	1.651
[6,6] - open	68-80	7.7	2.163	7.9	2.146
[5,6] - open	79-80	8.1	1.964	9.8	1.990
[5,6] - open	67-68	8.5	2.040	7.2	2.055
[6,6] - closed	28-29	9.0	1.661	9.2	1.661
[6,6] - closed	10-11	9.1	1.580	9.3	1.580
[6,6] - closed	3-12	9.5	1.577	9.6	1.577
[5,6] - open	11-12	9.7	2.140	9.7	2.141
[6,6] - closed	13-14	9.9	1.706	9.9	1.701
[6,6] - open	66-67	15.3	2.087	13.3	2.089
[5,6] - open	1-3 (*Expt*.)	18.7	2.070	18.9	2.073

[a] Relative energies in kcal mol^{-1} and bond distances in Å at the PBE0/TZP/D3 level. [b] Labels for the carbon atoms according to Figure 4b. The experimental (*Expt*.) structure U@C_s(4)-C_{82}Ad(I) is bond 1-3 (B1-3).

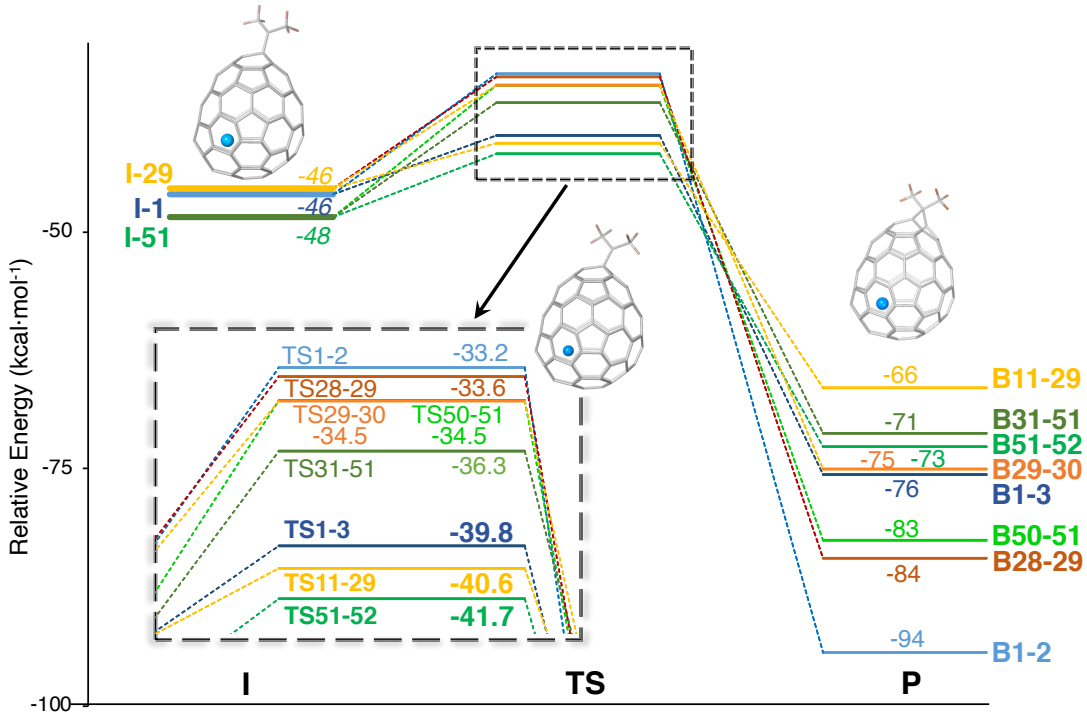

Figure 8. Energy profiles for carbene addition ($C(CH_3)_2$ model) on Th@C_s(4)-C_{82}, considering single-point energy calculations at the PBE0 level and solvent effects (toluene) with the PBE optimized geometry. Green, blue and yellow lines correspond to the I-51, I-1 and I-29 intermediates and, consequently, their reaction pathways. Relative energies (in kcal·mol^{-1}) for the intermediates (I), transition states (TS) and products (P) are plotted. Each color indicates a reaction path that leads to one product named BX-Y. The product B1-3 is the experimental structure of M@C_s(4)-C_{82}Ad(I).

In the first step of the triplet carbene mechanism, the reaction intermediates were calculated at different levels of theory (Table S11). Note that the two intermediates I-1 and I-3 can proceed to the formation of M@C_s(4)-C_{82}Ad(I). Each intermediate has three different carbene conformations, indicated as A, B, and C, which lead to different products. The lowest-energy intermediate is the one in which the carbene is attached to carbon atom 51 (I-51), followed by I-1 and I-29 with relative energies of approximately 2 and 3 kcal·mol^{-1}, respectively. The results including solvent

effects gave several intermediates with relative energies of 3-4 kcal·mol^{-1}. All these low-energy intermediates were selected and recomputed with Ad, also resulting in I-51 being the most stable intermediate, followed by I-29, I-1, I-13 and I-67. As we obtained very small energy differences between the intermediates, we also calculated all the possible transition states related to the lowest-energy intermediates (Tables 4 and S12). The transition states with the lowest energies appear to be I-51B, I-29C and I-1A. Figure 8 shows the energy profiles for the $C(CH_3)_2$ carbene addition on Th@C_s(4)-C_{82}, considering the reaction paths from I-59, I-29 and I-1. We note that the intermediate I-1A evolves to one of the transition states with the lowest relative energy to lead to the experimental product on bond B1-3. The intermediates I-51B and I-29C reaching products B51-52 and B11-29, respectively, are also competitive, which is in accordance with the experimental detection of more than one monoadduct. Energy barriers are rather low, in line with reactivity at ambient temperature once the carbene is photogenerated. It is remarkable that the intermediate on atom 1, I-1, could evolve to the thermodynamic product (bond B1-2) overcoming an energy barrier of 12.8 kcal mol^{-1} or to the kinetic product on bond B1-3 through a low-energy TS at only 6.2 kcal mol^{-1}. The lower distortion of the cage in the TS structure and the superior cage-carbene interaction explain the preference for bond B1-3 over the thermodynamic B1-2 bond. Test calculations using other functionals were performed, obtaining analogous results (Table S13). Therefore, our calculations show that the formation of M@C_s(4)-C_{82}Ad(I) (M=Th, U) occurs via a kinetically controlled process. Moreover, we suggest that M@C_s(4)-C_{82}Ad(II) (M=Th, U) could be product B51-52 or B11-29.

For the singlet carbene reaction pathway, the mechanism is concerted. The most competitive sites were considered to calculate the corresponding transition states in the (open-shell) spin singlet configuration. In this case, the transition states were found to have lower energies than the reactants,

so the Gibbs free energies at room temperature were analyzed. The Gibbs free energy barriers are provided in Table S15. In accordance with the triplet carbene addition pathway, TS1-3 is one of the transition states with the lowest free energy, along with TS51-52 and TS29-30. Thus, these results also confirm that the formation of U@C_s(4)-C_{82}Ad(I) (M=Th, U) occurs via a kinetically controlled process.

Table 4. Relative Energies with respect to Reactants for the Different Intermediates (I), Transition States (TS) and Products (P), as well as the Energy Barriers (EB) of carbene addition on Th@C_s(4)-C_{82}.[a]

I-X[b]	Atom type	E_{rel} I	E_{rel} TS	EB	P	Bond type	E_{rel} P
I-1A	566	-46.2	-39.8	6.4	B1-3	[5,6]	-75.6
I-1B	566	-46.2	-33.2	12.9	B1-2	[6,6]	-94.3
I-51A	566	-48.4	-34.5	13.9	B50-51	[6,6]	-82.5
I-51B	566	-48.4	-41.7	6.7	B51-52	[5,6]	-72.6
I-51C	566	-48.4	-36.3	12.0	B31-51	[5,6]	-71.2
I-29A	566	-45.6	-33.6	12.0	B28-29	[6,6]	-84.4
I-29B	566	-45.4	-34.5	10.9	B29-30	[5,6]	-75.0
I-29C	566	-46.2	-40.6	5.6	B11-29	[5,6]	-66.4

[a] Relative energies in kcal·mol^{-1}. Data from single point energy calculations at the PBE0/COSMO (toluene as a solvent) level with the PBE optimized geometry using the $C(CH_3)_2$ model. [b] The carbon atom (X) numbering is according to Figure 4b.

Discussion

The experimental results of the two addition reactions of U@C_s(4)-C_{82} demonstrate its unusual chemical reactivity and regioselectivity, which has never been reported for other EMFs. Both the BH reaction and photochemical carbene addition on U@C_s(4)-C_{82} show high selectivity. For the

BH reaction, in particular, only one single mono-adduct was obtained. Moreover, both reactions took place at unexpected addition sites, which is different from previous predictions and reports. The BH reaction is a nucleophilic reaction, and the carbene reaction is a typical electrophilic reaction. Supposedly, the two addition sites of the two reactions would be distant from each other, as observed in previous studies.[42, 56] The BH reaction on closed-shell EMFs leads to cycloadducts, usually open fulleroids but also closed methanofullerenes, with the internal metal normally pointing to the addition site, both for mono-metallofullerenes and nitride clusterfullerenes. Interestingly and already noted by Yang, Xie and coworkers, if bromomalonate is added to a radical EMF, such as $M@C_{82}$ with M^{3+} metals, singly bonded monoadducts are mainly obtained, with the possibility of also having some cycloadduct regiosiomer.[60] For all the singly bonded adducts known thus far, the metal is placed far from the bromomalonate. In addition, BH products are obtained under kinetic control. In contrast, carbene addition is a reaction of a radical electrophile with closed-shell or radical EMFs. Consequently, the regioselectivity is expected to be lower than for BH. In all cases, open fulleroids are obtained with the metal placed near the addition sites, which usually show large negative charges in the pristine cage.

In this work, for U@C_s(4)-C_{82}, as shown in Figure 7b, both the BH reaction and carbene addition occurred in adjacent C-C bonds in the same hexagon ring, with the U atom placed far from the functionalized bonds. Actually, these addition sites, which are surrounded by four pentagonal rings, are among the carbon atoms with the largest tension, i.e., pyramidalization, on the carbon cage. Therefore, in this particular case, the reaction mechanisms seem to be more strain-driven rather than charge-controlled nucleophilic or electrophilic additions.

Our mechanism and energy profile are able to explain the high regioselectivity of the BH reaction (one single adduct) on U@C_s(4)-C_{82}, and the crystallographic structure of the mono-adduct

isomer agrees well with the predicted thermodynamic and kinetic product, with a rather low energy barrier (< 10 kcal mol^{-1}). Unusually, the addition site is far from the metal, which is stacked near a sumanene motif. Other positions of the uranium inside the pristine $C_s(4)$-C_{82} are much higher in energy (>20 kcal mol^{-1}), which indicates the important U-sumanene interaction in this cage. In particular, a significant orbital interaction between the fragments is at the origin of such stabilization according to preliminary calculations. For both the BH and the carbene addition, moving the U off this sumanene or external functionalization on the sumanene motif disrupts this very favorable U-sumanene interaction and leads to intermediates and products with higher energies (Figure 9). In addition, due to the radical character of the carbene, this latter reaction is less regioselective, and several transition states with low barriers are found within a few kcal mol^{-1}, in agreement with the two regioisomers observed for $C_s(4)$-C_{82}. Therefore, the characteristic reactivity of U@$C_s(4)$-C_{82} is likely a consequence of the strong actinide-sumanene interaction in this very particular cage. In contrast, carbene additions on cages U@$C_{2v}(9)$-C_{82} and Th@$C_{3v}(8)$-C_{82}, in which the actinide is not as fixed as in U@$C_s(4)$-C_{82}, showed the *expected* products with the actinide near the addition site.

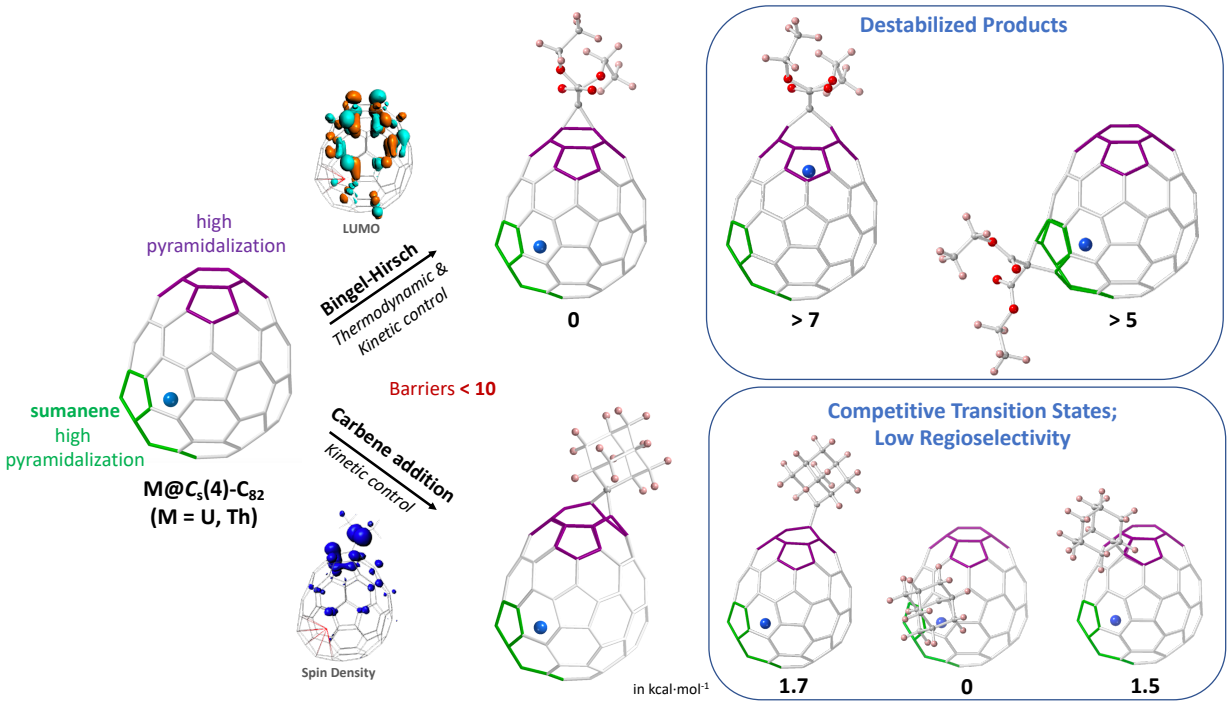

Figure 9. Bingel-Hirsch and carbene addition on U@C_s(4)-C_{82} lead to kinetically controlled products with barriers below 10 kcal mol^{-1}. The two reactions take place in the same region with C atoms showing high pyramidalization far from the metal atom, thus retaining the very favorable U-sumanene interaction present in the pristine cage. Lower regioselectivity is predicted for carbene addition, in line with the two products detected in the experiments.

Conclusion

In summary, a novel actinide EMF, U@C_s(4)-C_{82}, was successfully synthesized, and its molecular structure was unambiguously determined by single-crystal X-ray diffraction analysis. Crystallographic analysis show that U@C_s(4)-C_{82}, a new isomer of U@C_{82} has a C_s(4)-C_{82} cage, which has never been discovered in the form of empty or endohedral fullerenes. The unique chemical reactivities of U@C_s(4)-C_{82} were further revealed by investigations through the Bingel-Hirsch reaction and photochemical carbene addition, both of which usually show high regioselectivity toward U@C_s(4)-C_{82}. In particular, U@C_s(4)-C_{82} presents exceptionally high

selectivity with only one reaction product and high product yield (72%) for the BH reaction. This adduct is found to be both the thermodynamic and kinetic product of the BH reaction. In contrast to previous reports of carbene additions on M@C_{82}, where addition takes place at the most pyramidalized and negatively charged carbon atoms near the metal, the addition site in U@C_s(4)-C_{82}-Ad(I) is on carbon atoms with large pyramidalization and is far from the uranium atom. In addition, this carbene adduct is not the thermodynamic product, which indicates that this radical reaction is kinetically controlled with a lower regioselectivity than in the BH reaction, in line with experimental results.

For both reactions, the addition sites are located unexpectedly on adjacent carbon atoms far away from the actinide metal, despite the nucleophilic (Bingel-Hirsch) and electrophilic (carbene addition) nature of either reactant. DFT calculations suggest that this characteristic reactivity of U@C_s(4)-C_{82} is originated essentially from the unusually strong U-sumanene interaction, which prevents the motion of the actinide inside the cage. Thus, U@C_s(4)-C_{82} is a rare example of regioselectivity control by means of the metal-cage interaction. This study reveals unique molecular structure, as well as, unusual chemical properties of actinide EMFs and the critical role of the encapsulated actinide metal ion in the determination of their chemical behavior, which is beneficial for their future applications.

Experimental section

Synthesis of U@C_s(4)-C_{82}, U@C_s(4)-$C_{82}C(COOC_2H_5)_2$ and U@C_s(4)-C_{82}Ad(I, II).

U@C_s(4)-C_{82}: Uranium-based endohedral metallofullerenes were produced by a modified Krätschmer–Huffman DC arc discharge method.[61] Graphite rods packed with U_3O_8 and graphite powder (molar ratio of U: C = 1:30) were vaporized in the arcing chamber under a 200 Torr He atmosphere and 4 Torr N_2. The resulting soot was then collected and extracted with CS_2 for 12 h.

Multistage high-performance liquid chromatography (HPLC) separation processes were employed to isolate and purify U@C_s(4)-C_{82}.

U@C_s(4)-C_{82}C($COOC_2H_5$)$_2$: The Bingel-Hirch reaction of U@C_{82} (3 mg, 2.5 μmol) with diethyl bromomalonate (0.75 μL, 4.4 μmol) was conducted at room temperature in the presence of 1,8-diazabicyclo[5.4.0]undec-7-ene (DBU) (0.2 μL, 1.3 μmol) in dry toluene under N_2. The reaction proceeded very readily over 2 h. The crude reaction mixture was filtered to remove a small amount of precipitate and separated by multistage separation on HPLC.

U@C_s(4)-C_{82}Ad(I, II): AdN_2 was synthesized and purified as previously reported.[62-63] In a typical procedure, 3 mg of U@C_s(4)-C_{82} and an excess of AdN_2 were dissolved in 10 mL of anhydrous toluene, and the mixture was degassed by freeze–pump–thaw cycles under reduced pressures and then irradiated with an ultrahigh pressure mercury-arc lamp (cutoff < 350 nm) at room temperature. The reaction was monitored by analytical HPLC. The two isomers U@C_s(4)-C_{82}Ad(I) and U@C_s(4)-C_{82}Ad(II) were isolated from the unreacted starting materials by one-step HPLC.

X-ray Crystallographic Study

U@C_s(4)-C_{82}: Black block crystals of U@C_s(4)-C_{82}·[Ni^{II}-OEP] were obtained by slow diffusion of a benzene solution of Ni^{II}-OEP into a carbon disulfide solution of the metallofullerene sample. X-ray data were collected at 134 K using a diffractometer (Bruker D8 Venture) equipped with a CCD collector. The multiscan method was used for absorption correction. The structures were solved using direct methods[64] and refined on F^2 using full-matrix least-squares using the SHELXL2014 crystallographic software package.[65] Hydrogen atoms were inserted at calculated positions and constrained with isotropic thermal parameters.

Crystal data for U@C_s(4)-C_{82}·[Ni^{II}-OEP]·$(C_6H_6)_2$: Mr = 1970.52, 0.10 × 0.08 × 0.06 mm^3, triclinic, space group $P\bar{1}$ (No. 2), a = 14.5346(13) Å, b = 14.6294(11) Å, c = 19.9470(17) Å, α = 87.071(5)°,

β = 85.902(5)°, γ = 63.214(5)°, V = 3775.7(6) Å^3, Z = 2, ϱ_{calcd} = 1.773 g cm^{-3}, μ(Ga Kα) = 6.088 mm^{-1}, θ = 1.932-54.485°, T = 134 K, R_1 = 0.1405, wR_2 = 0.2825 for all data; R_1 = 0.1000, wR_1 = 0.2615 for 9366 reflections (I > 2.0σ(I)) with 1250 parameters. Goodness of fit indicator 1.061. The maximum residual electron density is 3.036 e Å^{-3}.

U@*C*$_s$(4)-C$_{82}$C(COOC$_2$H$_5$)$_2$: Black block crystals of U@*C*$_s$(4)-C$_{82}$C(COOC$_2$H$_5$)$_2$·1.5(CS$_2$) were obtained by liquid–liquid bilayer diffusion methods of a solution of U@*C*$_s$(4)-C$_{82}$C(COOC$_2$H$_5$)$_2$ in CS$_2$ and hexane as the poor solvent. X-ray data were collected at 120 K using a diffractometer (Bruker D8 Venture) equipped with a CCD collector. The multiscan method was used for absorption correction. The structures were solved using direct methods[64] and refined on F^2 using full-matrix least-squares using the SHELXL2014 crystallographic software package.[65] Hydrogen atoms were inserted at calculated positions and constrained with isotropic thermal parameters.

Crystal data for U@*C*$_s$(4)-C$_{82}$C(COOC$_2$H$_5$)$_2$·1.5(CS$_2$): C$_{90.5}$H$_{10}$O$_4$S$_3$U, *Mr* = 1495.19, 0.10 × 0.07 × 0.04 mm^3, tetragonal, space group *P* 4$_1$ 2$_1$ 2 (No. 92), a = 15.0154(17) Å, b = 15.0154(17) Å, c = 43.005(5) Å, α = 90°, β = 90°, γ = 90°, V = 9696(2) Å^3, Z = 8, ϱ_{calcd} = 2.049 g cm^{-3}, μ(Ga Kα) = 8.019 mm^{-1}, θ = 2.712-56.956°, T = 120(2) K, R_1 = 0.0522, wR_2 = 0.1140 for all data; R_1 = 0.0440, wR_1 = 0.1091 for 8918 reflections (I > 2.0σ(I)) with 925 parameters. Goodness of fit indicator 1.065. The maximum residual electron density is 1.249 e Å^{-3}.

U@*C*$_s$(4)-C$_{82}$Ad(I): Black block crystals of U@*C*$_s$(4)-C$_{82}$Ad were obtained by liquid–liquid bilayer diffusion methods of a solution of U@*C*$_s$(4)-C$_{82}$C(COOC$_2$H$_5$)$_2$ in CS$_2$ and hexane as the poor solvent. X-ray data were collected at 127 K using a diffractometer (Bruker D8 Venture) equipped with a CCD collector. The multiscan method was used for absorption correction. The structures were solved using direct methods[64] and refined on F^2 using full-matrix least-squares using the

SHELXL2014 crystallographic software package.[65] Hydrogen atoms were inserted at calculated positions and constrained with isotropic thermal parameters.

Crystal data for U@C_s(4)-C_{82}Ad: $C_{110}H_{18}U$, Mr = 1504.05, 0.12 × 0.1 × 0.08 mm^3, orthorhombic, space group P 2_1 2_1 2_1 (No. 19), a = 11.3660(10) Å, b = 18.8343(12) Å, c = 23.017(2) Å, α = 90°, β = 90°, γ = 90°, V = 4927.4(7) Å^3, Z = 4, ϱ_{calcd} = 2.027 g cm^{-3}, μ(Ga Kα) = 7.725 mm^{-1}, θ = 2.637-53.983°, T = 127 K, R_1 = 0.1123, wR_2 = 0.2588 for all data; R_1 = 0.0876 wR_1 = 0.2384 for 6422 reflections (I > 2.0σ(I)) with 921 parameters. Goodness of fit indicator 1.057. The maximum residual electron density is 1.598 e Å^{-3}.

Computational details. Amsterdam Density Functional (ADF, v. 2019) package[66] was employed for the Kohn-Sham density functional theory (DFT) calculations. The PBE0 exchange correlation functional[67-69] was used for optimizations of the Bingel-Hirsch and carbene addition products, whereas the PBE[67-68] was employed for reactants, intermediates, transition states and selected products. In addition, the PBE optimized geometries of all these stationary points were recomputed as single point energy calculations using the PBE0 functional and with an implicit solvent model. Solvent effects were introduced by means of the COnductor like Screening MOdel (COSMO), as implemented in ADF using toluene as a solvent.[70] All-electron triple-ζ polarized (TZP) Slater-type orbital (STO) basis sets quality were employed.[71-72] The scalar relativistic (SR) zero-order regular approximation (ZORA)[73] was included for relativistic effects, and the 'D3' dispersion corrections by Grimme were also considered.[74-75]

ASSOCIATED CONTENT

Supporting Information

This material is available free of charge via the Internet at http://pubs.acs.org.

HPLC profiles for the separation of U@C_s(4)-C_{82}; MS profiles for U@C_s(4)-$C_{82}C(COOC_2H_5)_2$ and U@C_s(4)-C_{82}Ad(I, II), experimental details; and complementary results from computations on U@C_s(4)-C_{82}, U@C_s(4)-$C_{82}C(COOC_2H_5)_2$ and U@C_s(4)-C_{82}Ad(I, II) (PDF)

Accession Codes

CCDC 2259113, 2259116 and 2259117 contain the supplementary crystallographic data for this paper. These data can be obtained free of charge via www.ccdc.cam.ac.uk/data_request/cif, by emailing data_request@ccdc.cam.ac.uk, or by contacting The Cambridge Crystallographic Data Centre, 12 Union Road, Cambridge CB2 1EZ, UK; fax: +44 1223 336033.

AUTHOR INFORMATION

Corresponding Author

Ning Chen – *College of Chemistry, Chemical Engineering and Materials Science, and State Key Laboratory of Radiation Medicine and Protection, Soochow University, Suzhou, Jiangsu 215123, P. R. China;* orcid.org/0000-0002-9405-6229; E-mail: chenning@suda.edu.cn

Antonio Rodríguez-Fortea – *Departament de Química Física i Inorgànica. Universitat Rovira i Virgili, Marcel·lí Domingo 1, 43007 Tarragona, Spain;* orcid.org/0000-0001-5884-5629; E-mail: antonio.rodriguezf@urv.cat

Author Contributions

$^{\perp}$Qin Wang and Laura Abella contributed equally.

Funding Sources

NSFC NO. 52172051, BK20200041, PID2020-112762GB-I00, 2021SGR00110

Notes

The authors declare no competing financial interests.

ACKNOWLEDGMENT

N. C. thanks the National Science Foundation China (NSFC NO. 52172051), the NSF of Jiangsu Province (BK20200041), and the Priority Academic Program Development of Jiangsu Higher Education Institutions (PAPD). A.R.-F. and J.M.P. thank the Spanish Ministry of Science and Innovation (grant PID2020-112762GB-I00 funded by MCIN/AEI/10.13039/501100011033), the Generalitat de Catalunya (grant 2021SGR00110) and the URV for support.

REFERENCES

(1) Popov, A. A.; Yang, S.; Dunsch, L. Endohedral Fullerenes. *Chem. Rev.* **2013**, *113* (8), 5989–6113.

(2) Yang, S.; Wei, T.; Jin, F. When metal clusters meet carbon cages: endohedral clusterfullerenes. *Chem. Soc. Rev.* **2017**, *46* (16), 5005–5058.

(3) Rodríguez-Fortea, A.; Balch, A. L.; Poblet, J. M. Endohedral metallofullerenes: a unique host–guest association. *Chem. Soc. Rev.* **2011**, *40* (7), 3551–3563.

(4) Lu, X.; Feng, L.; Akasaka, T.; Nagase, S. Current status and future developments of endohedral metallofullerenes. *Chem. Soc. Rev.* **2012**, *41* (23), 7723–7760.

(5) Aoyagi, S.; Nishibori, E.; Sawa, H.; Sugimoto, K.; Takata, M.; Miyata, Y.; Kitaura, R.; Shinohara, H.; Okada, H.; Sakai, T.; Ono, Y.; Kawachi, K.; Yokoo, K.; Ono, S.; Omote, K.; Kasama, Y.; Ishikawa, S.; Komuro, T.; Tobita, H. A layered ionic crystal of polar Li@C_{60} superatoms. *Nat. Chem.* **2010**, *2* (8), 678–683.

(6) Hu, Y.; Li, F.-F. Chemical Reactions of Endohedral Metallofullerenes. *Handbook of Fullerene Science and Technology*. **2021**, pp 1–32.

(7) Zhang, K.; Wang, C.; Zhang, M.; Bai, Z.; Xie, F.-F.; Tan, Y.-Z.; Guo, Y.; Hu, K.-J.; Cao, L.; Zhang, S.; Tu, X.; Pan, D.; Kang, L.; Chen, J.; Wu, P.; Wang, X.; Wang, J.; Liu, J.; Song, Y.; Wang, G.; Song, F.; Ji, W.; Xie, S.-Y.; Shi, S.-F.; Reed, M. A.; Wang, B. A $Gd@C_{82}$ single-molecule electret. *Nat. Nanotech.* **2020**, *15* (12), 1019–1024.

(8) Zhen, M.; Shu, C.; Li, J.; Zhang, G.; Wang, T.; Luo, Y.; Zou, T.; Deng, R.; Fang, F.; Lei, H.; Wang, C.; Bai, C. A highly efficient and tumor vascular-targeting therapeutic technique with size-expansible gadofullerene nanocrystals. *Sci. China Mater.* **2015**, *58* (10), 799–810.

(9) Mikawa, M.; Kato, H.; Okumura, M.; Narazaki, M.; Kanazawa, Y.; Miwa, N.; Shinohara, H. Paramagnetic Water-Soluble Metallofullerenes Having the Highest Relaxivity for MRI Contrast Agents. *Bioconjugate Chem.* **2001**, *12* (4), 510–514.

(10) Nie, H.; Zhao, C.; Shi, Z.; Jia, C.; Guo, X. Single-Molecule Fullerenes: Current Stage and Perspective. *ACS Mater. Lett.* **2022**, *4* (6), 1037–1052.

(11) Li, Y.; Zhao, Y.; Chen, Q.; Yang, Y.; Liu, Y.; Hong, Z.; Liu, Z.; Hsieh, Y.-T.; Meng, L.; Li, Y.; Yang, Y. Multifunctional Fullerene Derivative for Interface Engineering in Perovskite Solar Cells. *J. Am. Chem. Soc.* **2015**, *137* (49), 15540–15547.

(12) Bolskar, R. D.; Benedetto, A. F.; Husebo, L. O.; Price, R. E.; Jackson, E. F.; Wallace, S.; Wilson, L. J.; Alford, J. M. First Soluble $M@C_{60}$ Derivatives Provide Enhanced Access to Metallofullerenes and Permit in Vivo Evaluation of $Gd@C_{60}[C(COOH)_2]_{10}$ as a MRI Contrast Agent. *J. Am. Chem. Soc.* **2003**, *125* (18), 5471–5478.

(13) Jin, P.; Li, Y.; Magagula, S.; Chen, Z. Exohedral functionalization of endohedral metallofullerenes: Interplay between inside and outside. *Coord. Chem. Rev.* **2019**, *388*, 406–439.

(14) Chaur, M. N.; Melin, F.; Athans, A. J.; Elliott, B.; Walker, K.; Holloway, B. C.; Echegoyen, L. The influence of cage size on the reactivity of trimetallic nitride metallofullerenes: a mono- and bis-methanoadduct of $Gd_3N@C_{80}$ and a monoadduct of $Gd_3N@C_{84}$. *Chem. Commun.* **2008**, 2665–2667.

(15) Wang, Y.; Morales-Martinez, R.; Zhang, X.; Yang, W.; Wang, Y.; Rodriguez-Fortea, A.; Poblet, J. M.; Feng, L.; Wang, S.; Chen, N. Unique Four-Electron Metal-to-Cage Charge Transfer of Th to a C_{82} Fullerene Cage: Complete Structural Characterization of Th@C_{3v}(8)-C_{82}. *J. Am. Chem. Soc.* **2017**, *139* (14), 5110–5116.

(16) Cai, W.; Abella, L.; Zhuang, J.; Zhang, X.; Feng, L.; Wang, Y.; Morales-Martinez, R.; Esper, R.; Boero, M.; Metta-Magana, A.; Rodriguez-Fortea, A.; Poblet, J. M.; Echegoyen, L.; Chen, N. Synthesis and Characterization of Non-Isolated-Pentagon-Rule Actinide Endohedral Metallofullerenes U@C_1(17418)-C_{76}, U@C_1(28324)-C_{80}, and Th@C_1(28324)-C_{80}: Low-Symmetry Cage Selection Directed by a Tetravalent Ion. *J. Am. Chem. Soc.* **2018**, *140* (51), 18039–18050.

(17) Yan, Y.; Morales-Martinez, R.; Zhuang, J.; Yao, Y. R.; Li, X.; Poblet, J. M.; Rodriguez-Fortea, A.; Chen, N. Th@D_{5h}(6)-C_{80}: a highly symmetric fullerene cage stabilized by a single metal ion. *Chem. Commun.* **2021**, *57* (54), 6624–6627.

(18) Yao, Y. R.; Rosello, Y.; Ma, L.; Puente Santiago, A. R.; Metta-Magana, A.; Chen, N.; Rodriguez-Fortea, A.; Poblet, J. M.; Echegoyen, L. Crystallographic Characterization of U@C_{2n} (2n = 82-86): Insights about Metal-Cage Interactions for Mono-metallofullerenes. *J. Am. Chem. Soc.* **2021**, *143* (37), 15309–15318.

(19) Cai, W.; Morales-Martínez, R.; Zhang, X.; Najera, D.; Romero, E. L.; Metta-Magaña, A.; Rodríguez-Fortea, A.; Fortier, S.; Chen, N.; Poblet, J. M.; Echegoyen, L. Single crystal structures

and theoretical calculations of uranium endohedral metallofullerenes (U@C_{2n}, 2n = 74, 82) show cage isomer dependent oxidation states for U. *Chem. Sci.* **2017**, *8* (8), 5282–5290.

(20) Liu, X.; Li, B.; Yang, W.; Yao, Y. R.; Yang, L.; Zhuang, J.; Li, X.; Jin, P.; Chen, N. Synthesis and characterization of carbene derivatives of Th@C_{3v}(8)-C_{82} and U@C_{2v}(9)-C_{82}: exceptional chemical properties induced by strong actinide-carbon cage interaction. *Chem. Sci.* **2020**, *12* (7), 2488–2497.

(21) Khamatgalimov, A. R.; Kovalenko, V. I. Electronic Structure and Stability of Fullerene C_{82} Isolated-Pentagon-Rule Isomers. *J. Phy. Chem. A* **2011**, *115* (44), 12315–12320.

(22) Sun, G.; Kertesz, M. Identification for IPR Isomers of Fullerene C_{82} by Theoretical 13C NMR Spectra Calculated by Density Functional Theory. *J. Phy. Chem. A* **2001**, *105* (22), 5468–5472.

(23) Yang, S.; Wei, T.; Troyanov, S. I. A New Isomer of Pristine Higher Fullerene C_s-C_{82}(4) Captured by Chlorination as $C_{82}Cl_{20}$. *Chem– Asian J.* **2013**, *8* (2), 351–353.

(24) Bingel, C. Cyclopropanierung von Fullerenen. *Chem. Ber.* **1993**, *126* (8), 1957–1959.

(25) Hirsch, A.; Lamparth, I.; Groesser, T.; Karfunkel, H. R. Regiochemistry of Multiple Additions to the Fullerene Core: Synthesis of a Th-Symmetric Hexakis adduct of C_{60} with Bis(ethoxycarbonyl)methylene. *J. Am. Chem. Soc.* **1994**, *116* (20), 9385–9386.

(26) Hirsch, A.; Lamparth, I.; Karfunkel, H. R. Fullerene Chemistry in Three Dimensions: Isolation of Seven Regioisomeric Bisadducts and Chiral Trisadducts of C60 and Di(ethoxycarbonyl)methylene. *Angew. Chem., Int. Ed. Engl.* **1994**, *33* (4), 437–438.

(27) He, R.; He, R.; Xing, G.; Xing, G.; Wang, X.; Wang, X.; Jiao, Y.; Jiao, Y.; Zhao, H.; Zhao, H.; Yuan, H.; Yuan, H.; Wang, S.; Wang, S.; Dong, J.; Dong, J.; Lei, H.; Lei, H. Synthesis and

Evaluation of Bingel-Hirsch Multiadducts of Paramagnetic Gadofullerene as Potential Magnetic Resonance Imaging Contrast Agents. *J. Nanosci. Nanotechnol.* **2013**, *13* (2), 1549–1554.

(28) Shu, C.-Y.; Wang, C.-R.; Zhang, J.-F.; Gibson, H. W.; Dorn, H. C.; Corwin, F. D.; Fatouros, P. P.; Dennis, T. J. S. Organophosphonate Functionalized Gd@C_{82} as a Magnetic Resonance Imaging Contrast Agent. *Chem. Mater.* **2008**, *20* (6), 2106–2109.

(29) Feng, L.; Tsuchiya, T.; Wakahara, T.; Nakahodo, T.; Piao, Q.; Maeda, Y.; Akasaka, T.; Kato, T.; Yoza, K.; Horn, E.; Mizorogi, N.; Nagase, S. Synthesis and Characterization of a Bisadduct of La@C_{82}. *J. Am. Chem. Soc.* **2006**, *128* (18), 5990–5991.

(30) Feng, L.; Nakahodo, T.; Wakahara, T.; Tsuchiya, T.; Maeda, Y.; Akasaka, T.; Kato, T.; Horn, E.; Yoza, K.; Mizorogi, N.; Nagase, S. A Singly Bonded Derivative of Endohedral Metallofullerene: La@C_{82}CBr($COOC_2H_5$)$_2$. *J. Am. Chem. Soc.* **2005**, *127* (49), 17136–17137.

(31) Shen, W.; Yang, L.; Li, B.; Jin, P.; Yu, B.; Cong, H.; Akasaka, T.; Lu, X. Metal-encapsulation induces a highly regioselective Bingel-Hirsch reaction of the labile Y@C_s(6)-C_{82}. *Chem. Commun.* **2020**, *56* (92), 14357–14360.

(32) Pinzón, J. R.; Zuo, T.; Echegoyen, L. Synthesis and Electrochemical Studies of Bingel–Hirsch Derivatives of M_3N@I_h-C_{80} (M=Sc, Lu). *Chem. Eur. J.* **2010**, *16* (16), 4864–4869.

(33) Pinzón, J. R.; Cardona, C. M.; Herranz, M. Á.; Plonska-Brzezinska, M. E.; Palkar, A.; Athans, A. J.; Martín, N.; Rodríguez-Fortea, A.; Poblet, J. M.; Bottari, G.; Torres, T.; Gayathri, S. S.; Guldi, D. M.; Echegoyen, L. Metal Nitride Cluster Fullerene M_3N@C_{80} (M=Y, Sc) Based Dyads: Synthesis, and Electrochemical, Theoretical and Photophysical Studies. *Chem.Eur. J.* **2009**, *15* (4), 864–877.

(34) Cardona, C. M.; Elliott, B.; Echegoyen, L. Unexpected Chemical and Electrochemical Properties of M_3N@C_{80} (M = Sc, Y, Er). *J. Am. Chem. Soc.* **2006**, *128* (19), 6480–6485.

(35) Alegret, N.; Chaur, M. N.; Santos, E.; Rodriguez-Fortea, A.; Echegoyen, L.; Poblet, J. M. Bingel-Hirsch reactions on non-IPR $Gd_3N@C_{2n}$ (2n = 82 and 84). *J. Org. Chem.* **2010**, *75* (23), 8299–8302.

(36) Alegret, N.; Salvado, P.; Rodriguez-Fortea, A.; Poblet, J. M. Bingel-Hirsch addition on non-isolated-pentagon-rule $Gd_3N@C_{2n}$ (2n = 82 and 84) metallofullerenes: products under kinetic control. *J. Org. Chem.* **2013**, *78* (19), 9986–9990.

(37) Yang, S.; Chen, C.; Li, X.; Wei, T.; Liu, F.; Wang, S. Bingel–Hirsch monoadducts of $TiSc_2N@I_h$-C_{80} versus $Sc_3N@I_h$-C_{80}: reactivity improvement via internal metal atom substitution. *Chem. Commun.* **2013**, *49* (92), 10844–10846.

(38) Wang, S.; Huang, J.; Gao, C.; Jin, F.; Li, Q.; Xie, S.; Yang, S. Singly Bonded Monoadduct rather than Methanofullerene: Manipulating the Addition Pattern of Trimetallic Nitride Clusterfullerene through One Endohedral Metal Atom Substitution. *Chem.Eur. J.* **2016**, *22* (24), 8309–8315.

(39) Cai, T.; Xu, L.; Shu, C.; Reid, J. E.; Gibson, H. W.; Dorn, H. C. Synthesis and Characterization of a Non-IPR Fullerene Derivative: $Sc_3N@C_{68}[C(COOC_2H_5)_2]$. *J. Phy. Chem. C* **2008**, *112* (49), 19203–19208.

(40) Cai, T.; Xu, L.; Shu, C.; Champion, H. A.; Reid, J. E.; Anklin, C.; Anderson, M. R.; Gibson, H. W.; Dorn, H. C. Selective Formation of a Symmetric $Sc_3N@C_{78}$ Bisadduct: Adduct Docking Controlled by an Internal Trimetallic Nitride Cluster. *J. Am. Chem. Soc.* **2008**, *130* (7), 2136-2137.

(41) He, R.; Zhao, H.; Liu, J.; Jiao, Y.; Liang, Y.; Li, X.; Chen, C. Synthesis and Aggregation Studies of Bingel-Hirsch Monoadducts of Gadofullerene. *Fullerenes, Nanotubes, Carbon Nanostruct.* **2013**, *21* (6), 549–559.

(42) Feng, L.; Wakahara, T.; Nakahodo, T.; Tsuchiya, T.; Piao, Q.; Maeda, Y.; Lian, Y.; Akasaka, T.; Horn, E.; Yoza, K.; Kato, T.; Mizorogi, N.; Nagase, S. The Bingel monoadducts of La@C_{82}: synthesis, characterization, and electrochemistry. *Chem*. **2006**, *12* (21), 5578–5586.

(43) Pinzon, J. R.; Zuo, T.; Echegoyen, L. Synthesis and electrochemical studies of Bingel-Hirsch derivatives of $M_3N@I_h$-C_{80} (M=Sc, Lu). *Chem*. **2010**, *16* (16), 4864–4869.

(44) Garcia-Borras, M. C., M. R. Osuna, S. Izquierdo, M.; Luis, J. M. E., L. Sola, M. The Regioselectivity of Bingel-Hirsch Cycloadditions on Isolated Pentagon Rule Endohedral Metallofullerenes. *Angew*. *Chem*. *Int*. *Ed*. *Engl*. **2016**, *55* (7), 2374–2377.

(45) Alegret, N.; Rodriguez-Fortea, A.; Poblet, J. M. Bingel-Hirsch addition on endohedral metallofullerenes: kinetic versus thermodynamic control. *Chem*. *Eur*. *J*. **2013**, *19* (16), 5061–5069.

(46) Besalu-Sala, P.; Luis, J. M.; Sola, M. Bingel-Hirsch Addition of Diethyl Bromomalonate to Ion-Encapsulated Fullerenes M@C_{60} (M=Ø, Li^+, Na^+, K^+, Mg^{2+}, Ca^{2+}, and Cl^-). *Chem*. *Eur*. *J*. **2020**, *26* (63), 14481–14487.

(47) Zhao, P.; Dang, J. S.; Zhao, X. Bingel-Hirsch reaction mechanisms on $TiSc_2N@I_h$-C_{80}: the role of endohedral titanium nitride. *Phys*. *Chem*. *Chem*. *Phys*. **2016**, *18* (14), 9709–9714.

(48) Martinez, J. P.; Garcia-Borras, M.; Osuna, S.; Poater, J.; Bickelhaupt, F. M.; Sola, M. Reaction Mechanism and Regioselectivity of the Bingel-Hirsch Addition of Dimethyl Bromomalonate to La@C_{2v}-C_{82}. *Chem*. *Eur*. *J*. **2016**, *22* (17), 5953–5962.

(49) Li, Q.-Z.; Zheng, J.-J.; Zhao, X. Bingel–Hirsch Reaction on $Sc_2@C_{66}$: A Highly Regioselective Bond Neighboring to Unsaturated Linear Triquinanes. *J*. *Phy*. *Chem*. *C* **2015**, *119* (46), 26196–26201.

(50) Deng, Q.; Popov, A. A. Prato and Bingel-Hirsch cycloaddition to heptagon-containing $LaSc_2N@C_s$(hept)-C_{80}: importance of pentalene units. *Chem*. *Commun*. **2015**, *51* (26), 5637–5640.

(51) Hachiya, M.; Nikawa, H.; Mizorogi, N.; Tsuchiya, T.; Lu, X.; Akasaka, T. Exceptional Chemical Properties of Sc@C_{2v}(9)–C_{82} Probed with Adamantylidene Carbene. *J. Am. Chem. Soc.* **2012**, *134* (37), 15550–15555.

(52) Takano, Y.; Aoyagi, M.; Yamada, M.; Nikawa, H.; Slanina, Z.; Mizorogi, N.; Ishitsuka, M. O.; Tsuchiya, T.; Maeda, Y.; Akasaka, T.; Kato, T.; Nagase, S. Anisotropic Magnetic Behavior of Anionic Ce@C_{82} Carbene Adducts. *J. Am. Chem. Soc.* **2009**, *131* (26), 9340–9346.

(53) Lu, X.; Nikawa, H.; Feng, L.; Tsuchiya, T.; Maeda, Y.; Akasaka, T.; Mizorogi, N.; Slanina, Z.; Nagase, S. Location of the Yttrium Atom in Y@C_{82} and Its Influence on the Reactivity of Cage Carbons. *J. Am. Chem. Soc.* **2009**, *131* (34), 12066–12067.

(54) Akasaka, T.; Kono, T.; Takematsu, Y.; Nikawa, H.; Nakahodo, T.; Wakahara, T.; Ishitsuka, M. O.; Tsuchiya, T.; Maeda, Y.; Liu, M. T. H.; Yoza, K.; Kato, T.; Yamamoto, K.; Mizorogi, N.; Slanina, Z.; Nagase, S. Does Gd@C_{82} Have an Anomalous Endohedral Structure? Synthesis and Single Crystal X-ray Structure of the Carbene Adduct. *J. Am. Chem. Soc.* **2008**, *130* (39), 12840–12841.

(55) Akasaka, T.; Kono, T.; Matsunaga, Y.; Wakahara, T.; Nakahodo, T.; Ishitsuka, M. O.; Maeda, Y.; Tsuchiya, T.; Kato, T.; Liu, M. T. H.; Mizorogi, N.; Slanina, Z.; Nagase, S. Isolation and Characterization of Carbene Derivatives of La@C_{82}(C_s). *J. Phy. Chem. A* **2008**, *112* (6), 1294–1297.

(56) Maeda, Y.; Matsunaga, Y.; Wakahara, T.; Takahashi, S.; Tsuchiya, T.; Ishitsuka, M. O.; Hasegawa, T.; Akasaka, T.; Liu, M. T. H.; Kokura, K.; Horn, E.; Yoza, K.; Kato, T.; Okubo, S.; Kobayashi, K.; Nagase, S.; Yamamoto, K. Isolation and Characterization of a Carbene Derivative of La@C_{82}. *J. Am. Chem. Soc.* **2004**, *126* (22), 6858–6859.

(57) Zhang, W.; Suzuki, M.; Xie, Y.; Bao, L.; Cai, W.; Slanina, Z.; Nagase, S.; Xu, M.; Akasaka, T.; Lu, X. Molecular structure and chemical property of a divalent metallofullerene Yb@C_2(13)-C_{84}. *J. Am. Chem. Soc.* **2013**, *135* (34), 12730−12735.

(58) Haddon, R. C. Chemistry of the Fullerenes: The Manifestation of Strain in a Class of Continuous Aromatic Molecules. *Science* **1993**, *261* (5128), 1545−1550.

(59) Yamada, M.; Akasaka, T.; Nagase, S. Carbene Additions to Fullerenes. *Chem. Rev.* **2013**, *113* (9), 7209−7264.

(60) Wang, S.; Huang, J.; Gao, C.; Jin, F.; Li, Q.; Xie, S.; Yang, S. Singly Bonded Monoadduct rather than Methanofullerene: Manipulating the Addition Pattern of Trimetallic Nitride Clusterfullerene through One Endohedral Metal Atom Substitution. *Chem.* **2016**, *22* (24), 8309−8315.

(61) Krätschmer, W.; Lamb, L. D.; Fostiropoulos, K.; Huffman, D. R. Solid C_{60}: a new form of carbon. Nature 1990, 347, 354−358

(62) Schneider, Y.; Prévost, J.; Gobin, M.; Legault, C. Y. Diazirines as Potent Electrophilic Nitrogen Sources: Application to the Synthesis of Pyrazoles. *Org. Lett.* **2014,** *16* (2), 596−599.

(63) Ye, Q.; Komarov, I. V.; Kirby, A. J.; Jones, M. 3,5,7-Trimethyl-1-azatricyclo[3.3.1.13,7]decan-2-ylidene, an Aminocarbene without π Conjugation. *J. Org. Chem.* **2002,** *67* (26), 9288−9294.

(64) Dolomanov, O. V.; Bourhis, L. J.; Gildea, R. J.; Howard, J. A. K.; Puschmann, H. OLEX2: a complete structure solution, refinement and analysis program. *J. Appl. Crystallogr.* **2009,** *42* (2), 339−341.

(65) Sheldrick, G. Crystal structure refinement with SHELXL. *Acta Crystallogr., Sect. C* **2015,** *71* (1), 3−8.

(66) G. te Velde, G.; Bickelhaupt, F. M.; Baerends, E. J.; Fonseca Guerra, C.; van Gisbergen, S. J. A.; Snijders, J. G.; Ziegler, T. Chemistry with ADF. *J. Comput. Chem.* **2001,** *22* (9), 931–967.

(67) Perdew, J. P.; Burke, K.; Ernzerhof, M. Generalized Gradient Approximation Made Simple. *Phys. Rev. Lett.* **1996,** *77* (18), 3865–3868.

(68) Perdew, J. P.; Burke, K.; Ernzerhof, M. Erratum Generalized Gradient Approximation Made Simple [Phys. Rev. Lett. 77, 3865 (1996)]. *Phys. Rev. Lett.* **1997,** *78* (7), 1396–1396.

(69) Adamo, C.; Barone, V. Toward reliable density functional methods without adjustable parameters: The PBE0 model. *J. Chem.l Phy.* **1999,** *110* (13), 6158–6170.

(70) Klamt, A. Conductor-like Screening Model for Real Solvents: A New Approach to the Quantitative Calculation of Solvation Phenomena. *J. Phy. Chem.* **1995,** *99* (7), 2224–2235.

(71) Perdew, J. P. Density-functional approximation for the correlation energy of the inhomogeneous electron gas. *Phy. Rev. B* **1986,** *33* (12), 8822–8824.

(72) Becke, A. D. Density functional calculations of molecular bond energies. *J. Chem. Phy.* **1986,** *84* (8), 4524–4529.

(73) Lenthe, E. v.; Baerends, E. J.; Snijders, J. G. Relativistic regular two - component Hamiltonians. *J. Chem. Phy.* **1993,** *99* (6), 4597–4610.

(74) Grimme, S.; Antony, J.; Ehrlich, S.; Krieg, H. A consistent and accurate ab initio parametrization of density functional dispersion correction (DFT-D) for the 94 elements H-Pu. *J. Chem. Phy.* **2010,** *132* (15), 154104–154122.

(75) Grimme, S.; Ehrlich, S.; Goerigk, L. Effect of the damping function in dispersion corrected density functional theory. *J. Comput. Chem.* **2011,** *32* (7), 1456–1465.

BRIEFS. The study of a novel EMF, U@C_s(4)-C_{82}, reveals the remarkable chemical properties of actinide endohedral metallofullerenes (EMFs). The addition sites for both nucleophilic (BH) and electrophilic (Carbene) reactions of U@C_s(4)-C_{82} are unexpectedly located on adjacent carbon atoms far way from the metal, representing a rare example of chemical reactivity control by means of the actinide-cage interaction.